

<https://doi.org/10.1038/s43246-024-00479-3>

Quantum simulation of an extended Dicke model with a magnetic solid

Check for updates

Nicolas Marquez Peraca^{1,14}, Xinwei Li² ✉, Jaime M. Moya^{1,3,14}, Kenji Hayashida^{4,5,14}, Dasom Kim^{3,5}, Xiaoxuan Ma⁶, Kelly J. Neubauer¹, Diego Fallas Padilla¹, Chien-Lung Huang^{1,7}, Pengcheng Dai¹, Andriy H. Nevidomskyy¹, Han Pu¹, Emilia Morosan^{1,8}, Shixun Cao⁶ ✉, Motoaki Bamba^{9,10,11,12} ✉ & Junichiro Kono^{1,5,13} ✉

The Dicke model describes the cooperative interaction of an ensemble of two-level atoms with a single-mode photonic field and exhibits a quantum phase transition as a function of light–matter coupling strength. Extending this model by incorporating short-range atom–atom interactions makes the problem intractable but is expected to produce new physical phenomena and phases. Here, we simulate such an extended Dicke model using a crystal of ErFeO_3 , where the role of atoms (photons) is played by Er^{3+} spins (Fe^{3+} magnons). Through terahertz spectroscopy and magnetocaloric effect measurements as a function of temperature and magnetic field, we demonstrated the existence of a novel atomically ordered phase in addition to the superradiant and normal phases that are expected from the standard Dicke model. Further, we elucidated the nature of the phase boundaries in the temperature–magnetic-field phase diagram, identifying both first-order and second-order phase transitions. These results lay the foundation for studying multiatomic quantum optics models using well-characterized many-body solid-state systems.

The Dicke model in quantum optics describes the cooperative, coherent coupling of an ensemble of two-level atoms with a single-mode light field¹. Despite its simplicity, the model hosts a rich variety of phenomena that are significant in diverse contexts, such as cavity quantum electrodynamics², condensed matter physics³, and quantum information science^{4,5}. A prominent feature of the model is a second-order quantum phase transition (QPT), known as the superradiant phase transition (SRPT), which occurs when the light–matter coupling strength, g , exceeds a threshold^{6,7}. When the system enters the superradiant phase, atomic and photonic polarizations spontaneously emerge, producing a unique many-body ground state that enables studies of unusual light–matter entanglement⁸, two-mode squeezed states^{9–11}, and quantum chaos¹².

Although the atomic ensemble in the original Dicke model was assumed to be noninteracting, it has been known from the early days that atom–atom interactions are important for explaining, for example, the dephasing and intensity correlation functions of fluorescent spectra^{13,14}. Hence, there has long been interest in extending the Dicke model to include an atom–atom interaction (represented by strength J); see Fig. 1. Such an extended Dicke model, or the g – J model, should display an interplay of two types of interatomic interactions – i.e., the photonic-field-mediated *long-range* interaction, and the direct *short-range* interaction. Intuitively, one can expect the ground state of the system to crucially depend on the ratio g/J , with a superradiant phase (an atomically ordered phase) favored for large (small) g/J . However, no analytical solutions can be obtained for the g – J

¹Department of Physics and Astronomy, Rice University, Houston, TX, USA. ²Department of Physics, California Institute of Technology, Pasadena, CA, USA.

³Applied Physics Graduate Program, Smalley–Curl Institute, Rice University, Houston, TX, USA. ⁴Division of Applied Physics, Graduate School of Engineering, Hokkaido University, Hokkaido, Japan. ⁵Department of Electrical and Computer Engineering, Rice University, Houston, TX, USA. ⁶Department of Physics, International Center of Quantum and Molecular Structures, and Materials Genome Institute, Shanghai University, Shanghai, China. ⁷Department of Physics and Center for Quantum Frontiers of Research and Technology, National Cheng Kung University, Tainan, Taiwan. ⁸Department of Chemistry, Rice University, Houston, TX, USA. ⁹Department of Physics I, Kyoto University, Kyoto, Japan. ¹⁰The Hakubi Center for Advanced Research, Kyoto University, Kyoto, Japan. ¹¹PRESTO, Japan Science and Technology Agency, Saitama, Japan. ¹²Department of Physics, Yokohama National University, Yokohama, Japan. ¹³Department of Materials Science and NanoEngineering, Rice University, Houston, TX, USA. ¹⁴These authors contributed equally: Nicolas Marquez Peraca, Jaime M. Moya, Kenji Hayashida.

✉ e-mail: xinweili@caltech.edu; sxcao@shu.edu.cn; bamba.motoaki.y13@kyoto-u.jp; kono@rice.edu

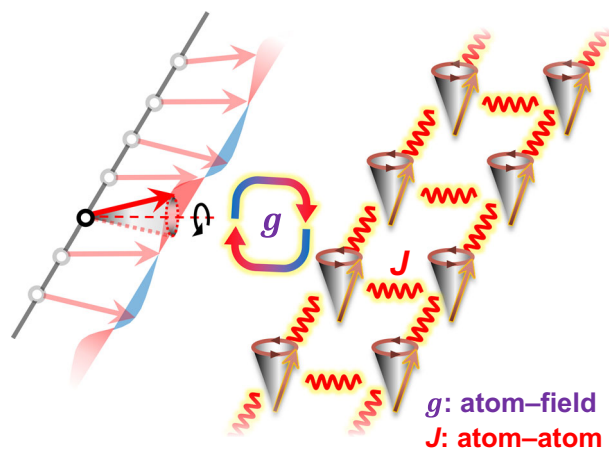


Fig. 1 | The extended Dicke model, or the g - J model, where an ensemble of interacting two-level atoms collectively couples with a bosonic field. The cooperative boson–atom interaction, with strength g , mediates long-range atom–atom interactions, whereas the direct atom–atom interaction, with strength J , is short-ranged.

model, motivating one to simulate it using a well-characterized many-body quantum system.

Computational studies of the g - J model under various approximations have revealed an array of new phenomena, such as a first-order QPT^{15–19}, a shift of the SRPT boundary^{20,21}, amplification of the integrability-to-chaos transition²², modifications of matter–matter entanglement^{20,23}, and alteration of the nature of an excited-state QPT^{18,24}. To examine these phenomena, several experimental platforms, including atomic Bose–Einstein condensates^{25,26}, superconducting qubits^{27,28}, and quantum dots¹⁵, have been proposed as quantum simulators, but successful simulations have not been achieved.

Here, we present a novel protocol of using a crystal of erbium orthoferrite (ErFeO_3), an antiferromagnetic (AFM) insulator, as a solid-state quantum simulator of the g - J model. The magnetic properties of ErFeO_3 are governed by the moments carried by the Er^{3+} and Fe^{3+} spin subsystems and their interplay²⁹. A previous study has revealed Dicke cooperativity in the Er^{3+} – Fe^{3+} interaction³⁰, demonstrating the resemblance of the magnetic Hamiltonian of ErFeO_3 to the Dicke Hamiltonian. Namely, the paramagnetic Er^{3+} ions (the magnons of ordered Fe^{3+} spins) play the role of the atomic ensemble (light field), and the spin–magnon interaction is formally similar to the g -term in the Dicke model. What further strengthens this analogy is a magnetic phase transition of the crystal that exhibits all traits that would be expected for a Dicke SRPT. When the temperature (T) becomes lower than 4 K, the Er^{3+} lattice develops C-type AFM order³¹ (with the ferromagnetic chains along z), and a zone-boundary Fe^{3+} magnon mode condenses, displacing the staggered moments away from the x - z plane^{32,33}; this corresponds to the emergence of atomic and photon polarizations in the standard SRPT. In Bertaut’s notation, the magnetic transition is of the $\Gamma_2 \rightarrow \Gamma_{12}$ type (Fig. 2a). Mean-field calculations using a realistic spin model captures the simultaneous order parameter (OP) onset of both the Er^{3+} and Fe^{3+} spin components, $\langle \Sigma_z^+ \rangle$ and $\langle S_z \rangle$, respectively (Fig. 2b), indicating that the $\Gamma_2 \rightarrow \Gamma_{12}$ transition is a magnonic SRPT³⁴, with the Γ_2 and Γ_{12} phases corresponding to the normal (N) and superradiant (S) phases, respectively.

Results

One way to observe the OP onset is to monitor the quasi-antiferromagnetic (qAFM) magnon mode of Fe^{3+} spins through terahertz (THz) time-domain spectroscopy, which has been utilized to reveal the configuration of Fe^{3+} ions in rare-earth orthoferrites³⁵. By performing THz transmission measurements on a z -cut ErFeO_3 crystal in the Faraday geometry, we obtained absorption coefficient (α) spectra, derived from the imaginary part of the refractive index (see Methods), as a function of T , as shown in Fig. 2c.

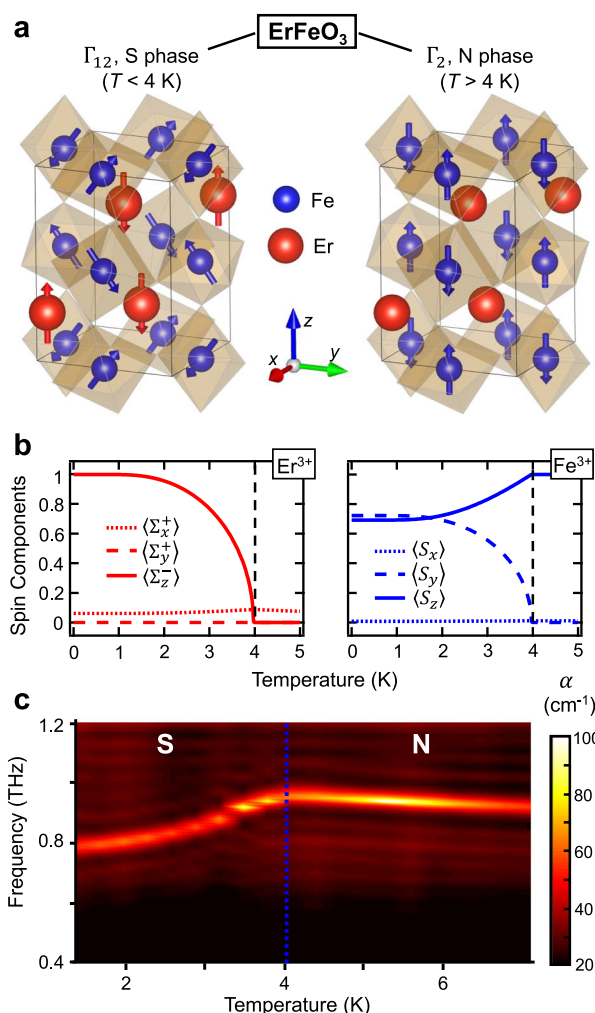


Fig. 2 | The $\Gamma_2 \rightarrow \Gamma_{12}$ transition in ErFeO_3 as a magnonic analog of the SRPT. **a** Lattice structure and spin configurations within the Γ_{12} and Γ_2 phases. Brown polyhedra represent octahedrally coordinated FeO_6 cages. **b** Temperature dependence of the Er^{3+} and Fe^{3+} spin components (normalized) across the phase transition at 0 T. $\hat{\Sigma}_p$, where $p \in \{x, y, z\}$, is the collective Er^{3+} spin operator, with its superscript “+” (“–”) denoting the sum (difference) of the two sublattices. \hat{S}_p are the components of Fe^{3+} spins. **c** Temperature dependence of THz absorption spectra taken at zero magnetic field. The bright line, corresponding to the qAFM magnon mode of Fe^{3+} spins, shows a kink at 4 K, which is the superradiant-normal phase boundary at zero magnetic field.

The observed bright absorption line is the qAFM mode, which has been thoroughly studied in previous studies³⁵. It is the evolution of this mode in distinct phases of the g - J model that is of interest throughout this study. A continuous OP-like onset, or a kink, is observed at the N \rightarrow S transition boundary (< 4 K, blue dashed line). The frequency shift of the qAFM magnon mode in the S phase from that in the N phase is thus a sensitive reporter of the qAFM magnon condensate density, namely, the Fe^{3+} OP of the S phase.

The J -term is inherently built into the magnetic Hamiltonian of ErFeO_3 since the Er^{3+} – Er^{3+} exchange interaction, albeit being weak, is known to be present³⁶. Spectroscopic measurements have also revealed a fine frequency splitting within the Er^{3+} electron paramagnetic resonance lines³⁰, which is attributable to the Er^{3+} – Er^{3+} exchange interaction. The presence of both the g - and J -terms sets the stage for ErFeO_3 to simulate the g - J model. In the limit of strong interatomic interaction $J \gg g$, one expects to find an atomic (A) phase characterized by an interatomic OP, without the superradiant order. Nonetheless, although the g -term-driven S phase can find

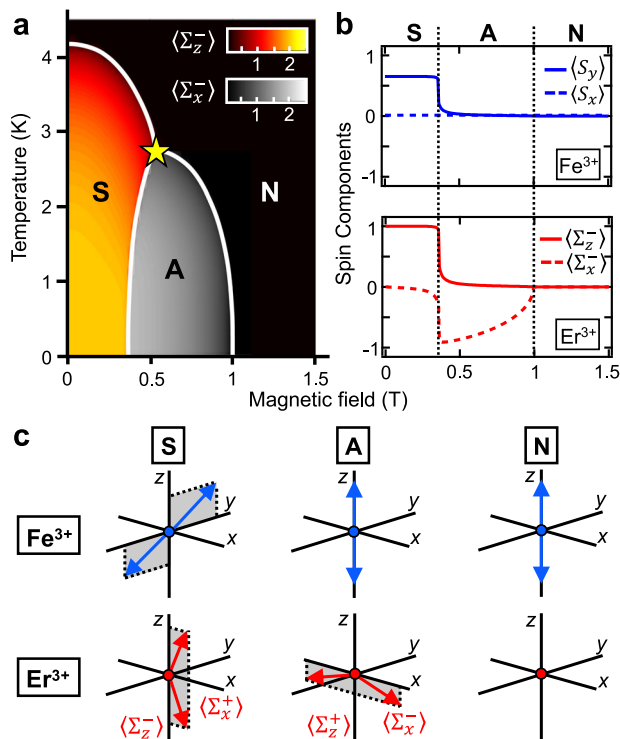


Fig. 3 | Mean-field solution for the spin Hamiltonian of ErFeO₃ in H||z. **a** Theoretical *T*-*H* phase diagram mapped by Er³⁺ spin components. **b** *H*-dependent evolution of the Er³⁺ and Fe³⁺ spin components (normalized) at *T* = 0 K. **c** Schematic diagrams of the spin configuration in each phase.

correspondence to the Γ₁₂ phase in ErFeO₃, the *g*/*J* ratio set for the crystal stipulates that a pure atomic (A) phase, which is driven exclusively by the *J*-term, would not appear in equilibrium. For ErFeO₃, the A phase would be an Er³⁺ ordered phase without involving any OP onset in the Fe³⁺ subsystem. Therefore, to achieve quantum simulation of the *g*-*J* model, we must search for a way to invoke an explicit A phase through an S → A transition.

Our theoretical consideration suggests that subjecting ErFeO₃ to a static magnetic field (*H*) along the *z* axis can potentially induce an S → A transition. This can be understood by writing the simplified magnetic Hamiltonian (see Methods) in the second-quantized form as

$$\hat{H}/\hbar = \omega_{\pi} \hat{a}_{\pi}^{\dagger} \hat{a}_{\pi} + \omega_{\text{Er}} \hat{\Sigma}_x^{+} + \omega_z \hat{\Sigma}_z^{+} + g \sqrt{\frac{2}{N_0}} i (\hat{a}_{\pi}^{\dagger} - \hat{a}_{\pi}) \hat{\Sigma}_z^{-} + J \frac{6}{N_0 \hbar} \left[(\hat{\Sigma}_x^{+})^2 + (\hat{\Sigma}_z^{+})^2 - (\hat{\Sigma}_x^{-})^2 - (\hat{\Sigma}_z^{-})^2 \right], \quad (1)$$

where a two-sublattice approximation is adopted for both Er³⁺ and Fe³⁺ for a total of *N*₀ unit cells. Here, ω_π, â_π[†], and â_π are the energy, creation, and annihilation operators for the Fe³⁺ qAFM magnon mode, respectively; ω_{Er} is the frequency of Er³⁺ spins as two-level systems at *H* = 0; ω_z = |g_zμ_Bμ₀*H*|/ħ, where g_z is the Landè *g* factor, μ_B is the Bohr magneton, and μ₀ is the vacuum permeability, is the *H*-induced Zeeman frequency of Er³⁺; and *g* and *J* are the Er³⁺-magnon and Er³⁺-Er³⁺ coupling strengths, leading to the *g*- and *J*-terms of the *g*-*J* Hamiltonian, respectively. $\hat{\Sigma}_p = \sum_{i=1}^{2N_0} \hat{\sigma}_{i,p} / 2$, where $\hat{\sigma}_p$ are Pauli matrices and *p* ∈ {*x*, *y*, *z*}, is the collective Er³⁺ spin operator, with its superscript “+” (“-”) denoting the sum (difference) of the two sublattices. The way these operators appear in Eq. (1) is crucial for interpreting the ground-state energetics. Specifically, the *g*-term features a product of the Fe³⁺ magnon field operator *i*(â_π[†] - â_π) and the Σ_z⁻ component of Er³⁺ spins, thereby favoring antiparallel alignment of Er³⁺ sublattices and Fe³⁺ magnon condensation in the S phase (the onsets of ⟨Σ_z⁻⟩ and ⟨S_y⟩ in Fig. 2b), whereas the *J*-term couples Er³⁺ antiferromagnetically; larger ⟨Σ_x⁻⟩ and ⟨Σ_z⁻⟩, where ⟨...⟩ denotes expectation values, are energetically more favorable.

It is important to note that supplying the Zeeman term $\hat{H}_{\text{Zeeman}}/\hbar = \omega_z \hat{\Sigma}_z^{+}$ provides quantum controllability. The term promotes |Σ_z⁺⟩, the net moment of Er³⁺ sublattices, through Zeeman coupling to *H*||*z*. Due to the commutation relation

$$[\hat{\Sigma}_z^{+}, \hat{\Sigma}_z^{-}] = 0 \neq [\hat{\Sigma}_z^{+}, \hat{\Sigma}_x^{-}], \quad (2)$$

modification to ⟨Σ_z⁺⟩ would impact ⟨Σ_x⁻⟩ much more than ⟨Σ_z⁻⟩. This would tip the balance between the *g*-term and the *J*-term, since Σ_x⁻ appears only in the *J*-term but not in the *g*-term.

As shown in Fig. 3a, an S → A transition is indeed recovered in the calculated mean-field phase diagram of the spin Hamiltonian (see Methods) within the *T*-*H* parameter space, for *T* < 2.8 K, with a critical field ranging from 0.35 T to 0.5 T, depending on *T*. Increasing the field to above 1 T and elevating *T* to above 4 K would both push the system across the thermodynamic phase boundary into the N phase. A triple point (at 2.8 K and 0.5 T, decorated by a yellow star) marks the location where the S, A, and N phases converge. Figure 3b shows the calculated normalized spin components as the OPs of the magnetic phases, for a line cut along the *H* axis at *T* = 0 K, traversing sequentially the S → A and the A → N boundaries. We identify that the Fe³⁺ OP, represented by ⟨S_y⟩, is finite in the S phase but near-zero in the A phase. The Er³⁺ OP, on the other hand, is finite in both the S and A phases, but undergoes a switch from the ⟨Σ_z⁻⟩ ≠ 0, ⟨Σ_x⁻⟩ ≈ 0 type (S phase) to the ⟨Σ_z⁻⟩ ≈ 0, ⟨Σ_x⁻⟩ ≠ 0 type (A phase). Further, the OP evolution indicates that the S → A boundary is an abrupt-type, first-order phase transition, while the A → N boundary is a continuous-type, second-order phase transition.

Summarizing the mean-field calculation results, Fig. 3c pictorially shows the predicted Fe³⁺ and Er³⁺ spin order in each phase. Starting from the N phase, the two sublattices of Fe³⁺ are antiparallel along *z* with zero *y*-component, while Er³⁺ spins remain paramagnetic (no order). The A phase is characterized by Fe³⁺ order that is identical to that of the N phase, but the Er³⁺ subsystem develops canted AFM order where the sublattice moments are antiparallel along *x* (⟨Σ_x⁻⟩ ≠ 0), with canting along *z* (⟨Σ_z⁺⟩ ≠ 0). In the S phase, the Er³⁺ order takes the ⟨Σ_x⁺⟩ ≠ 0, ⟨Σ_z⁻⟩ ≠ 0 configuration, and the staggered moment of the Fe³⁺ sublattices undergoes a rotation about the *x* axis, bringing its *y*-component to nonzero.

The S → A transition can be considered as a spin-flop transition in terms of Er³⁺ ions. One conventional way to characterize the transition is to monitor the magnetic susceptibility through which the existence of the AFM ordering of Er³⁺ spins in the A phase has been previously observed³⁷, although the configuration of Fe³⁺ spins was left ambiguous. Our magnetization measurements showed clear S → A and S → N phase boundaries (squares in Fig. 4a and Supplementary Fig. 1). However, a strong and non-uniform demagnetizing effect that broadens the phase boundary³⁸ likely prevented us from clearly identifying the A → N phase boundary. This is because the shape of our sample for magnetization measurements was a thin irregularly shaped disk cut from the sample used for THz measurements, rather than a sphere, which would have produced a uniform demagnetizing field inside the sample³⁷. Nonetheless, a disk-shaped sample with a large lateral size was necessary for performing THz transmission measurements.

To demonstrate the A → N phase boundary, i.e., the breakdown of the AFM order of Er³⁺ spins, we performed magnetocaloric effect (MCE) experiments which are sensitive to the magnetic entropy landscape of a material. Namely, the Grüneisen ratio³⁹

$$\Gamma_H = - \frac{(\partial S / \partial H)_T}{C_H} = \frac{1}{T} \frac{\partial T}{\partial H} \Big|_S, \quad (3)$$

measures the slope of isentropes in the *T*-*H* plane⁴⁰. Since the heat capacity C_H is always a positive quantity, the sign of (∂*T*/∂*H*)_S is always opposite to (∂*S*/∂*H*)_T. Furthermore, sharp changes in entropy *S* due to phase transitions will appear as step functions in (∂*T*/∂*H*)_S⁴⁰, or peaks if (∂*T*/∂*H*) is measured in a quasi-

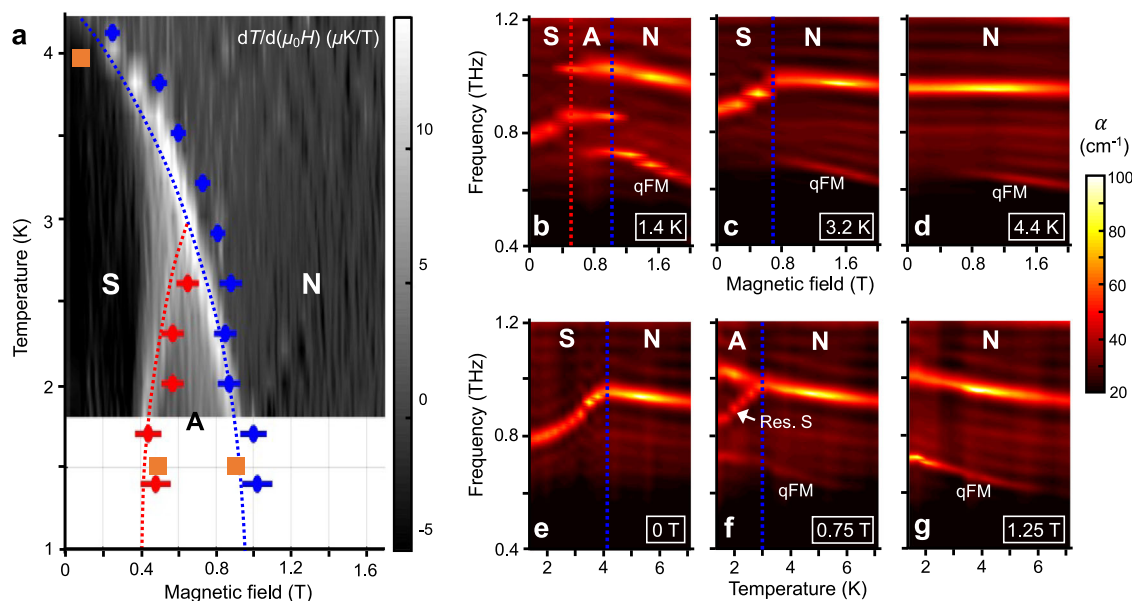


Fig. 4 | Mapping out the T - H phase diagram of ErFeO_3 in $H\parallel z$. **a** Phase boundaries determined by THz measurements (solid circles) and magnetization measurements (squares) overlaid on the $dT/d(\mu_0H)$ color map determined from MCE measurements. Red (blue) dashed line denotes a first- (second-) order phase boundary.

b–d THz absorption spectra mapped vs μ_0H for select T values. **e–g** THz absorption spectra mapped vs T for select μ_0H values. Red and blue dashed lines mark the same boundaries as those in (a). All features except for those labeled “qFM” are qAFM magnon modes of Fe^{3+} spins.

adiabatic environment⁴¹. Thus, by measuring the differential change in sample temperature with respect to the magnetic field, $(\frac{\partial T}{\partial H})_S$, the T - H magnetic phase diagram can be measured. We note that the demagnetization factor can have a small effect on the MCE measurements⁴², namely that temperature and field shifts can occur, but the qualitative features should be present.

The T - H phase diagram of ErFeO_3 , and the obtained results are summarized in Fig. 4a. We configured a MCE measurement in a Physical Property Measurement System in the quasi-adiabatic condition⁴³, and took raw data traces of sample temperature variation versus magnetic field at a ramping rate of 5×10^{-3} T/s with $dH > 0$ (Supplementary Fig. 2a); the sensitivity of temperature variation of our instrument reached 5×10^{-4} K. To identify H -induced phase transitions, the first-order derivative $(\frac{\partial T}{\partial H})_S$ was approximated as $dT/d(\mu_0H)$ (Supplementary Fig. 2b), whose local extremes correspond to the transition boundaries⁴¹. The traces clearly exhibit two maxima for $T < 2.8$ K, corresponding to the $S \rightarrow A$ (red dashed line in Fig. 4a) and $A \rightarrow N$ (blue dashed line) boundaries, and one maximum for $2.8 \text{ K} < T < 4$ K, corresponding to the $S \rightarrow N$ (blue dashed line) boundary. These results are qualitatively consistent with the T - H phase diagram reported previously³⁷, where quantitative shifts likely come from demagnetization effects.

Once we experimentally investigated the evolution of the atomic ensemble (or the Er^{3+} spins) in the extended Dicke Hamiltonian, we turned to elucidate the photonic counterpart (or the Fe^{3+} spins). The ambiguity of the configuration of Fe^{3+} spins and the nature of the transition boundaries require us to monitor the qAFM magnon mode of Fe^{3+} spins in THz magnetospectroscopy experiments. Unlike the static measurements, responses from different domains in the A phase can be distinguished in the frequency domain, illuminating the nature of the phase transition. The measurements were performed within the same T - H parameter space as that of the MCE experiments. Figure 4b–d and e–g shows the H -dependence of α spectra at select T values and the T -dependence of α spectra at select μ_0H values, respectively. We found that the bright absorption lines can be assigned to either the quasi-ferromagnetic (qFM) mode or the qAFM mode³⁵, the latter of which can be an OP for the Fe^{3+} spins.

In the H -dependent color map at 1.4 K (Fig. 4b), three lines are observed. The lowest frequency line, which does not pick up intensity until 0.8 T, is the qFM mode, while the other two are both qAFM magnons, albeit

belonging to distinct phases. The middle (upper) line, which is located at 0.8 THz at 0 T (1 THz at 0.5 T), is the qAFM mode of the S (A & N) phase. The $S \rightarrow A$ transition can be identified to occur at 0.5 T (red dashed line), where the upper line emerges. The qAFM magnons belonging to the S and A phases coexist within $0.5 \text{ T} < \mu_0H < 1 \text{ T}$, consistent with the prediction that the $S \rightarrow A$ transition is of first order and is thus inhomogeneous, until the middle line vanishes at $> 1 \text{ T}$ (blue dashed line) owing to entrance into the N phase. The 3.2 K map (Fig. 4c) shows a different behavior; the qAFM magnon (0.88 THz at 0 T) of the S phase continuously shifts to connect with that of the N phase in frequency, forming an OP-like onset for $\mu_0H < 0.7 \text{ T}$ (blue dashed line), signaling a second-order $N \rightarrow S$ transition boundary. Such a frequency shift is absent in the 4.4 K map (Fig. 4d) since the N phase persists throughout the whole H range.

T -dependent color maps at constant H further corroborate our assignments of the phase transitions. Again from the 0 T map (Fig. 4e), a continuous OP-like onset of the qAFM mode shift is observed (< 4 K, blue dashed line). This echoes Fig. 4c in showing the continuous nature of the $N \rightarrow S$ transition, and establishes that the frequency shift of the qAFM magnon in the S phase from that in the N phase can be the Fe^{3+} OP of the S phase. Intriguingly, this OP is demonstrated to be zero in the A phase. We read this fact from the 0.75 T map (Fig. 4f), for which an $N \rightarrow A$ transition is expected upon lowering T . Although a residual mode pertaining to the S phase exists (as mentioned earlier when discussing Fig. 4b), the qAFM mode (unlabeled line) frequency does not undergo any noticeable OP-like anomaly across the $N \rightarrow A$ transition; it is as featureless as the qAFM mode within the 1.25 T map (Fig. 4g), for which the N phase persists throughout the whole T range. This unambiguously demonstrates that the spin order in the A phase only involves Er^{3+} ordering but not any Fe^{3+} OP, consistent with our expectation depicted in Fig. 3. Finally, phase boundaries determined by the THz experiments are overlaid (as solid circles) on top of the MCE phase diagram in Fig. 4a, showing overall agreement.

Discussion

A potential impact of this analogy is the possibility of being applied to other members of the rare-earth orthoferrite family or orthochromite compounds. For example, spin-reorientation phase transitions^{44,45} ($\Gamma_4 \rightarrow \Gamma_2$) in RFeO_3 ($\text{R} = \text{Yb}, \text{Er}, \text{and Tb}$) would mimic the SRPT. In YbFeO_3 , where the Yb^{3+} - Yb^{3+} interaction (J) is negligible, it would be a potential playground for

studying the standard Dicke model (g model). At the boundaries of the phase transition of YbFeO_3 , the qFM mode of Fe^{3+} shows a kink, and a transition inside the ground doublet of Yb^{3+} ions shows a softening⁴⁶. This simultaneous kink and softening is one of the hallmarks of a magnonic SRPT⁴⁷. It was also suggested that TbFeO_3 can be regarded as the magnetic phase transition of the Jahn-Teller type^{48,49} that would resemble a magnonic SRPT. In ErFeO_3 , where a crystal field transition (~ 1.5 THz) is responsible for the spin-reorientation transition ($T = 87$ K), the crystal field levels would play the role of an ensemble of two-level atoms in the Dicke model. To prove that Dicke physics is at work, however, one must show Dicke cooperativity, i.e., the coupling strength g must exhibit cooperative enhancement $g \propto \sqrt{N}$, where N is the number of two-level atoms. In addition, mapping their spin Hamiltonians into the Dicke models is required to establish this analogy. No attempts have been made to develop an analogy between the spin-reorientation transition and the Dicke superradiant phase transition.

The advantages of using the low-temperature phase transition, as opposed to the ~ 80 K spin-reorientation phase transition, of ErFeO_3 in simulating the extended Dicke model can be summarized as follows. First, the low-temperature phase transition allows us to simulate the first-order phase transition into the A phase, which is the main point of this work and does not exist in the spin-reorientation transition at 87 K. Second, since we deal with the lowest two energy levels (Kramers doublet) of Er^{3+} ions in the low-temperature phase transition, theoretical analysis is directly relevant to the Dicke model, compared to the multiple crystal-field energy levels involved in the 87 K phase transition. Third, and most importantly, at high temperatures, thermally populated magnons are not negligible. Such thermal magnons will prevent studies of the vacuum magnons responsible for the Dicke superradiant phase transition, which occurs in thermal equilibrium without any external driving. For example, one consequence of the superradiant phase transition induced by vacuum bosonic fields is a two-mode perfect squeezed vacuum at the critical point³⁴. A finite number of thermally excited magnons will mask such interesting quantum phenomena.

Conclusion

In summary, through THz magnetospectroscopy and magnetocaloric effect experiments, we studied a crystal of ErFeO_3 to simulate the g - J model, which is an extended Dicke model that includes not only the bosonic-field-mediated long-range interatomic interactions but also direct short-range interatomic interactions. In addition to the superradiant and normal phases expected from the standard Dicke model, we identified a new phase, an atomic phase, which is driven by the short-range J -term in the Hamiltonian. Further, we elucidated the nature of the various phase boundaries, distinguishing between first-order and second-order transitions. These results demonstrated the potential of ErFeO_3 as a simulator of quantum optics Hamiltonians. More specifically, in the context of Dicke physics, this condensed matter platform may lead to the possibilities of assisting quantum chaos²² and modifying matter-matter entanglement^{20,23} with tunability given through an external magnetic field. Bridging the gap between quantum optics and many-body correlated physics, our results will find broader application in the design of hybrid quantum systems with superior controllability, such as the Dicke-Ising machine^{27,50} and the Dicke-Lipkin-Meshkov-Glick model^{18,23}. Furthermore, the ability to transition between the superradiant and atomic phases via a nonthermal knob provides opportunities to study unconventional quantum criticality⁵¹ and chaos-assisted thermalization⁵².

Methods

Spin Hamiltonian

Following the prior work³⁴, the spin Hamiltonian taking into account all the spin subsystems and their mutual interactions is first introduced. We analyzed the ErFeO_3 spin system from a microscopic model originally derived in ref. ³⁴. The total microscopic Hamiltonian is

$$\mathcal{H} = \mathcal{H}_{\text{Fe}} + \mathcal{H}_{\text{Er}} + \mathcal{H}_{\text{Fe-Er}}. \quad (4)$$

\mathcal{H}_{Fe} , \mathcal{H}_{Er} , and $\mathcal{H}_{\text{Fe-Er}}$ are Fe^{3+} , Er^{3+} , and Fe^{3+} - Er^{3+} interaction Hamiltonian, respectively. As in our previous studies^{30,53} and Herrmann's model⁵⁴, we take the two-sublattice model both for Er and Fe spins.

The Fe^{3+} Hamiltonian is

$$\begin{aligned} \mathcal{H}_{\text{Fe}} = & \sum_{s=A,B} \sum_{i=1}^{N_0} \mu_B \mu_0 \hat{S}_i^s \cdot \mathbf{g}^{\text{Fe}} H + J_{\text{Fe}} \sum_{\text{n.n.}} \hat{S}_i^A \cdot \hat{S}_i^B \\ & - D_y^{\text{Fe}} \sum_{\text{n.n.}} \left(\hat{S}_{i,z}^A \hat{S}_{i,x}^B - \hat{S}_{i,z}^B \hat{S}_{i,x}^A \right) \\ & - \sum_{i=1}^{N_0} \left(A_x \hat{S}_{i,x}^2 + A_z \hat{S}_{i,z}^2 + A_{xz} \hat{S}_{i,x}^A \hat{S}_{i,z}^A \right) \\ & - \sum_{i=1}^{N_0} \left(A_x \hat{S}_{i,x}^B + A_z \hat{S}_{i,z}^B - A_{xz} \hat{S}_{i,x}^B \hat{S}_{i,z}^B \right). \end{aligned}$$

\hat{S}_i^s is the Fe^{3+} spin operator with $S = 5/2$ at the i -th site and s sublattice. J_{Fe} , D_y^{Fe} , $A_{x(z,xz)}$ are a Fe^{3+} isotropic exchange constant, Dzyaloshinskii-Moriya interaction for the $y(b)$ -axis, and the single ion anisotropy for the $x(z, xz)$ spin components. $\sum_{\text{n.n.}}$ is a summation for the nearest neighbors and the number of nearest neighbors is $z_{\text{Fe}} = 6$. N_0 is the number of unit cells in ErFeO_3 . The g -factor of Fe^{3+} is

$$\mathbf{g}^{\text{Fe}} = \begin{pmatrix} g_x^{\text{Fe}} & 0 & 0 \\ 0 & g_y^{\text{Fe}} & 0 \\ 0 & 0 & g_z^{\text{Fe}} \end{pmatrix}.$$

μ_B is the Bohr magneton and H is an external magnetic field.

The Er^{3+} Hamiltonian is

$$\mathcal{H}_{\text{Er}} = \sum_{s=A,B} \sum_{i=1}^{N_0} \frac{\mu_0}{2} \hat{\sigma}_i^s \cdot \mathbf{g}^{\text{Er}} \cdot H + J_{\text{Er}} \sum_{\text{n.n.}} \hat{\sigma}_i^A \cdot \hat{\sigma}_i^B.$$

$\hat{\sigma}_i^s$ is the Er^{3+} spin operator at the i -th site and s sublattice. J_{Er} represents Er^{3+} - Er^{3+} isotropic exchange constant. The g -factor of Er^{3+} is

$$\mathbf{g}^{\text{Er}} = \begin{pmatrix} g_x & 0 & 0 \\ 0 & g_y & 0 \\ 0 & 0 & g_z \end{pmatrix}.$$

Finally, the Fe^{3+} - Er^{3+} interaction Hamiltonian is

$$\mathcal{H}_{\text{Er-Fe}} = \sum_{i=1}^{N_0} \sum_{s,s'=A,B} \left[J \hat{\sigma}_i^s \cdot \hat{S}^{s'} + D^{s,s'} \cdot \left(\hat{\sigma}_i^s \times \hat{S}^{s'} \right) \right].$$

In our Fe^{3+} - Er^{3+} interaction Hamiltonian, Fe^{3+} and Er^{3+} interact within the same unit cell. J is a Fe^{3+} - Er^{3+} isotropic exchange constant. $D^{s,s'}$ is the Dzyaloshinskii-Moriya interaction and

$$\begin{aligned} D^{A,A} &= (D_x, D_y, 0)^t, \\ D^{A,B} &= (-D_x, -D_y, 0)^t, \\ D^{B,A} &= (-D_x, D_y, 0)^t, \\ D^{B,B} &= (D_x, -D_y, 0)^t. \end{aligned}$$

The state of spins are determined by the equations of motion in which we assume each individual spin experiences a uniform mean field supplied by its surrounding magnetic ions. Assuming the dynamics within all unit

cells are identical, we can replace spins dependent on unit cells, S_i^s and σ_i^s , with uniform spins, S^s and σ^s keeping the sublattice dependence. From the Heisenberg equation from the Hamiltonian (Eq. (4)), the equations of motion are

$$\hbar \frac{\partial}{\partial t} \sigma^s = -\sigma^s \times \mu_0 g \mu_B H_{\text{Er}}^s(\{\sigma^{A/B}\}, \{S^{A/B}\}), \quad (5)$$

$$\hbar \frac{\partial}{\partial t} S^s = -S^s \times \mu_0 g \mu_B H_{\text{Fe}}^s(\{\sigma^{A/B}\}, \{S^{A/B}\}). \quad (6)$$

g is the free electron g -factor. H_{Er}^s and H_{Fe}^s are the mean-fields for Er^{3+} and Fe^{3+} spins, respectively. The mean-fields are defined as derivatives of the total Hamiltonian (Eq. (4)) with respect to the corresponding spin variables, for example $g\mu_0\mu_B H_{\text{Er}}^s = 2\partial\mathcal{H}/\partial\sigma^s$. The phase diagrams shown in Figs. 2 and 3 are calculated by the following procedure.

From the equations of motion, the equilibrium spins ($\bar{\sigma}^{A/B}$ and $\bar{S}^{A/B}$) are parallel to the mean-fields $\bar{H}_{\text{Er}}^s = H_{\text{Er}}^s(\{\bar{\sigma}^{A/B}\}, \{\bar{S}^{A/B}\})$ and $\bar{H}_{\text{Fe}}^s = H_{\text{Fe}}^s(\{\bar{\sigma}^{A/B}\}, \{\bar{S}^{A/B}\})$. They are connected as

$$\bar{\sigma}^s = \langle \hat{\sigma}^s \rangle = \langle \hat{\sigma}_{\parallel}^s \rangle u_{\text{Er}}^s, \quad \hat{\sigma}_{\parallel}^s = \hat{\sigma}^s \cdot u_{\text{Er}}^s, \quad u_{\text{Er}}^s = \bar{H}_{\text{Er}}^s / |\bar{H}_{\text{Er}}^s|, \quad (7)$$

$$\bar{S}^s = \langle \hat{S}^s \rangle = \langle \hat{S}_{\parallel}^s \rangle u_{\text{Fe}}^s, \quad \hat{S}_{\parallel}^s = \hat{S}^s \cdot u_{\text{Fe}}^s, \quad u_{\text{Fe}}^s = \bar{H}_{\text{Fe}}^s / |\bar{H}_{\text{Fe}}^s|. \quad (8)$$

We determine the equilibrium spins ($\bar{\sigma}^{A/B}$ and $\bar{S}^{A/B}$) in the following self-consistent equations

$$\langle \hat{\sigma}_{\parallel}^s \rangle = -\frac{\partial}{\partial y_s} \ln Z_{\text{Er}}^s = -\tanh(y_s), \quad (9)$$

$$\langle \hat{S}_{\parallel}^s \rangle = -\frac{\partial}{\partial x_s} \ln Z_{\text{Fe}}^s = -SB_S(Sx_s), \quad (10)$$

$B_j(z)$ is the Brillouin function

$$B_j(z) = \frac{2J+1}{2J} \coth\left(\frac{2J+1}{2J}z\right) - \frac{1}{2J} \coth\left(\frac{z}{2J}\right),$$

and the partition functions are

$$Z_{\text{Er}}^s \equiv \text{Tr} \left[e^{-\hat{\mathcal{H}}_{\text{Er}}^s / k_B T} \right] = \sum_{m=\pm 1} e^{-my_s} = 2 \cosh(y_s), \quad (11)$$

$$Z_{\text{Fe}}^s \equiv \text{Tr} \left[e^{-\hat{\mathcal{H}}_{\text{Fe}}^s / k_B T} \right] = \sum_{m=-S}^S e^{-mx_s} = \frac{\sinh[(S+1/2)x_s]}{\sinh(x_s/2)}, \quad (12)$$

$$y_s = \frac{g\mu_0\mu_B |\bar{H}_{\text{Er}}^s|}{2k_B T}, \quad x_s = \frac{g\mu_0\mu_B |\bar{H}_{\text{Fe}}^s|}{k_B T}.$$

k_B is Boltzmann constant and T is temperature. Finally, the effective Hamiltonians of given mean-fields \bar{H}_{Er}^s and \bar{H}_{Fe}^s are

$$\hat{\mathcal{H}}_{\text{Er}}^s = \frac{1}{2} g\mu_0\mu_B \hat{\sigma}^s \cdot \bar{H}_{\text{Er}}^s = \frac{1}{2} g\mu_0\mu_B \hat{\sigma}_{\parallel}^s |\bar{H}_{\text{Er}}^s|,$$

$$\hat{\mathcal{H}}_{\text{Fe}}^s = g\mu_0\mu_B \hat{S}^s \cdot \bar{H}_{\text{Fe}}^s = g\mu_0\mu_B \hat{S}_{\parallel}^s |\bar{H}_{\text{Fe}}^s|.$$

Here, $\hat{\sigma}^s$ and \hat{S}^s are vectors of the Pauli operators and angular momentum with the magnitude S .

To determine the ground state, we calculate free energy from the partition functions, Eqs. (11) and (12), and pick the configuration with the

lowest energy. The free energies are defined as

$$F_{\text{Er}}^s = -k_B T \ln Z_{\text{Er}}^s,$$

$$F_{\text{Fe}}^s = -k_B T \ln Z_{\text{Fe}}^s.$$

The total free energy of Er^{3+} and Fe^{3+} spins are

$$F = \sum_{s=A,B} (F_{\text{Er}}^s + F_{\text{Fe}}^s) / 2. \quad (13)$$

Extended Dicke model

Second quantization of the spin Hamiltonian Eq. (4) has been carried out by ref. ³⁴. We omit the derivation here since details can be found in the reference. For the sake of consistency, notation will follow those in ref. ³⁴, but will be substituted by those used in Eq. (1) eventually. Ref. ³⁴ expressed the total Hamiltonian as

$$\begin{aligned} \hat{\mathcal{H}} \approx & \sum_{K=0,\pi} \hbar \omega_K \hat{a}_K^\dagger \hat{a}_K + \omega_{\text{Er}} \hat{\Sigma}_x^+ + \sum_{\xi=x,y,z} g_{\xi}^{\text{Er}} \mu_B B_{\xi}^{\text{DC}} \hat{\Sigma}_{\xi}^+ \\ & + \frac{8z_{\text{Er}} J_{\text{Er}}}{N} \hat{\Sigma}^A \cdot \hat{\Sigma}^B + \frac{2\hbar g_x}{\sqrt{N}} (\hat{a}_{\pi}^\dagger + \hat{a}_{\pi}) \hat{\Sigma}_x^+ \\ & + \frac{i2\hbar g_y}{\sqrt{N}} (\hat{a}_0^\dagger - \hat{a}_0) \hat{\Sigma}_y^+ + \frac{2\hbar g_y'}{\sqrt{N}} (\hat{a}_{\pi}^\dagger + \hat{a}_{\pi}) \hat{\Sigma}_y^- \\ & + \frac{i2\hbar g_z}{\sqrt{N}} (\hat{a}_{\pi}^\dagger - \hat{a}_{\pi}) \hat{\Sigma}_z^- + \frac{2\hbar g_z'}{\sqrt{N}} (\hat{a}_0^\dagger + \hat{a}_0) \hat{\Sigma}_z^+. \end{aligned} \quad (14)$$

Here, $K=0$ and π corresponds to the qFM and qAFM magnon modes. $\hat{\Sigma}^{A/B}$ is a spin- $\frac{N}{4}$ operator representing the rare-earth spins in the A/B sublattice, satisfying

$$\hat{\Sigma}^{A/B} \equiv \frac{1}{2} \sum_{i=1}^{N_0} \hat{R}_i^{A/B}, \quad (15)$$

where $(1/2)\hat{R}_i^{A/B}$ is a spin- $\frac{1}{2}$ operator for an Er^{3+} ion. We also define the sum and difference of the two sublattice spins as

$$\hat{\Sigma}^{\pm} \equiv \hat{\Sigma}^A \pm \hat{\Sigma}^B. \quad (16)$$

The total number of spin- $\frac{1}{2}$ spins (Er^{3+} spins) in the two sublattices is

$$N \equiv 2N_0. \quad (17)$$

The five Er^{3+} -magnon coupling terms were rewritten in terms of the annihilation (creation) operators \hat{a}_K (\hat{a}_K^\dagger) of a magnon, with their respective coupling strengths defined as

$$\begin{aligned} \hbar g_x &= \sqrt{2S}(J \cos \beta_0 - D_y \sin \beta_0) \left(\frac{b+a}{d-c} \right)^{1/4} \\ &= h \times 0.051 \text{ THz}, \end{aligned} \quad (18a)$$

$$\begin{aligned} \hbar g_y &= \sqrt{2S}J \left(\frac{d+c}{b-a} \right)^{1/4} \\ &= h \times 0.041 \text{ THz}, \end{aligned} \quad (18b)$$

$$\begin{aligned} \hbar g_y' &= \sqrt{2S}(D_x \sin \beta_0) \left(\frac{b+a}{d-c} \right)^{1/4} \\ &= h \times 3.1 \times 10^{-5} \text{ THz}, \end{aligned} \quad (18c)$$

$$\begin{aligned} \hbar g_z &= \sqrt{2SD_x} \left(\frac{d-c}{b+a} \right)^{1/4} \\ &= h \times 0.116 \text{ THz}, \end{aligned} \quad (18d)$$

$$\begin{aligned} \hbar g'_z &= \sqrt{2S}(-J \sin \beta_0 - D_y \cos \beta_0) \left(\frac{b-a}{d+c} \right)^{1/4} \\ &= h \times (-0.040 \text{ THz}). \end{aligned} \quad (18e)$$

The numerical values of these coupling strengths are evaluated by the set of parameters, $a, b, c, d, J, \beta_0, D_x, D_y$, which are defined and quantitatively given in ref. ³⁴. We found that the $\hbar g_z$ is the dominant term, for which we retain in Eq. (1) and all other Fe^{3+} - Er^{3+} coupling terms are dropped as an approximation.

Regarding the Er^{3+} - Er^{3+} interaction term, while the Er^{3+} spin ensemble is described by six operators, $\hat{\Sigma}_{x,y,z}^+$ and $\hat{\Sigma}_{x,y,z}^-$, in the extended Dicke Hamiltonian, only $\hat{\Sigma}_x^+$ and $\hat{\Sigma}_z^-$ are relevant to the low-temperature phase transition. $\hat{\Sigma}_x^+$ corresponds to the paramagnetic alignment by the Fe^{3+} magnetization along the a axis, and $\hat{\Sigma}_z^-$ corresponds to the anti-ferromagnetic ordering along the c axis. Then, for analyzing the thermal-equilibrium values of the spins, we need to consider only the following terms in the Er^{3+} - Er^{3+} exchange interactions:

$$\begin{aligned} \frac{8z_{\text{Er}}J_{\text{Er}}}{N} \hat{\Sigma}^A \cdot \hat{\Sigma}^B &= \frac{2z_{\text{Er}}J_{\text{Er}}}{N} \sum_{\xi=x,y,z} \left[\left(\hat{\Sigma}_{\xi}^+ \right)^2 - \left(\hat{\Sigma}_{\xi}^- \right)^2 \right] \\ &\rightarrow \frac{2z_{\text{Er}}J_{\text{Er}}}{N} \left[\left(\hat{\Sigma}_x^+ \right)^2 + \left(\hat{\Sigma}_z^+ \right)^2 - \left(\hat{\Sigma}_x^- \right)^2 - \left(\hat{\Sigma}_z^- \right)^2 \right]. \end{aligned} \quad (19)$$

After this substitution, a notation substitution of $g_z \rightarrow g$ and $J_{\text{Er}} \rightarrow J$, and incorporating the aforementioned simplification about the coupling terms, Eq. (14) becomes Eq. (1). Numerical values of the material parameters therein are:

$$J = 0.037 \text{ meV} \quad (20)$$

$$g = 0.48 \text{ meV} \quad (21)$$

$$\omega_{\pi} = 2\pi \times 0.896 \text{ THz} \quad (22)$$

$$\omega_{\text{Er}} = 2\pi \times 0.023 \text{ THz}. \quad (23)$$

Sample preparation

Polycrystalline ErFeO_3 was first synthesized by a conventional solid state reaction method using Er_2O_3 (99.9%) and Fe_2O_3 (99.98%) powders. According to the stoichiometric ratio, the original reagents were weighted carefully and pulverized with moderate anhydrous ethanol in an agate mortar. Mixtures were sintered at 1300 °C for 1000 min and then cooled down to room temperature. The sintered powders were thoroughly reground and pressed into a rod that is 70 mm in length and 5–6 mm in diameter by a Hydrostatic Press System (Riken Seiki CO. Ltd, model HP-M-SD-200) at 70 MPa, and then sintered again at 1300 °C for sufficient reaction. Single crystal samples were then grown by an optical floating zone furnace (FZT-10000-H-VI-P-SH, Crystal Systems Corp; heat source: four 1 kW halogen lamps). The polycrystalline samples were melted in an airflow. Conditions like the melting power and the rate of sample rotation were stabilized and controlled in the molten zone.

Magnetization measurements

We measured iso-field (Supplementary Fig. 1a, left axis, blue circles) and isothermal (Supplementary Fig. 1b, left axis, blue circles) magnetization M to determine the phase transitions in the T - H plane of ErFeO_3 for magnetic

field $H \parallel c$. The transition from the $N \rightarrow S$ states is marked by the maximum in the derivative $d(MT)/dT$ ⁵⁵ (Supplementary Fig. 1a right axis, red squares). The transition from the $S \rightarrow A$ states in the isothermal M measured at $T = 1.5 \text{ K}$ (Supplementary Fig. 1b, left axis, blue circles) is clearly marked by the maximum in dM/dH (Supplementary Fig. 1b right axis, red triangles). The transition from the $A \rightarrow N$ states is much less obvious, marked by a small kink in dM/dH (Supplementary Fig. 1b right axis, red triangles) marked by the gray dashed lane. This may be due to demagnetization effects due to the irregularity of the sample shape we measured. Nonetheless, we are able to use MCE measurements that clearly exhibit signatures of the $A \rightarrow N$ transition. It is noted that transitions shown here from magnetization measurements are consistent within error bars with the T - H phase diagram presented in Fig. 4a.

THz magnetospectroscopy

We performed time-domain THz transmission magnetospectroscopy measurements in the Faraday geometry. The sample is placed in a liquid-helium-cooled magneto-optical cryostat (Oxford Instruments Spectromag-10T) with variable temperatures T between 1.4 and 300 K and static magnetic fields $\mu_0 H$ up to 10 T. We generate THz pulses via optical rectification using a Ti:sapphire regenerative amplifier (775 nm, 0.7 mJ, 150 fs, 1 kHz, Clark-MXR, Inc., CPA2001) as a laser source that pumps a (110) zinc telluride (ZnTe) crystal, while detection is accomplished through electro-optical sampling in another ZnTe crystal.

Index of refraction and absorption coefficient

In this section we derive the standard equations used in the extraction of the complex index of refraction of a sample using THz-TDS. Let $\tilde{E}_0(\omega)$ be the Fourier transform of an incoming THz pulse $E_0(t)$ incident on two linear media surrounding a homogeneous dielectric slab of thickness d (the sample). We assume that trailing pulses due to multiple reflections within the sample (the Fabry-Pérot effect) are well separated in time from the main transmitted THz pulse and that the incidence is normal to the sample surfaces (assumed parallel and flat). Experimentally, two separate measurements are consecutively carried out. First, the THz electric field transmitting without a sample in place is measured and the reference electric field $\tilde{E}_r(\omega)$ is obtained. Second, both the sample and its surroundings is measured and $\tilde{E}_s(\omega)$ is extracted. Under these assumptions, each transmitted electric field can be written as^{56,57}:

$$\tilde{E}_r(\omega) = \tilde{t}_{13}(\omega) \tilde{P}_{\text{vac}}(\omega, d) \tilde{E}_0(\omega) \quad (24)$$

$$\tilde{E}_s(\omega) = \tilde{t}_{12}(\omega) \tilde{P}_s(\omega, d) \tilde{t}_{23} \tilde{E}_0(\omega) \quad (25)$$

where $\tilde{t}_{jk} = \frac{2\tilde{n}_j}{\tilde{n}_j + \tilde{n}_k}$ is the complex Fresnel transmission coefficient between mediums j and k , $\tilde{P}_j(\omega, d_j) = e^{ik_0 d_j \tilde{n}_j} = e^{i(\omega d_j/c) \tilde{n}_j}$ is the propagator through medium j , and the subscripts vac, r, and s refer to vacuum, reference, and sample, respectively. The ratio between $\tilde{E}_r(\omega)$ and $\tilde{E}_s(\omega)$ is the transfer function $\tilde{H}(\omega)$, and it follows from Eqs. (24) and (25) that:

$$\tilde{H}(\omega) = \frac{\tilde{E}_s(\omega)}{\tilde{E}_r(\omega)} = \frac{\tilde{t}_{12} \tilde{t}_{23} \tilde{P}_s(\omega, d)}{\tilde{t}_{13} \tilde{P}_{\text{vac}}(\omega, d)} = \frac{2\tilde{n}_2(\tilde{n}_1 + \tilde{n}_3)}{(\tilde{n}_1 + \tilde{n}_2)(\tilde{n}_2 + \tilde{n}_3)} e^{i(\omega d/c)(\tilde{n}_s - 1)} \quad (26)$$

The bulk samples characterized in this work are single crystals grown without a substrate, and therefore, the surrounding mediums can be taken as vacuum by setting $\tilde{n}_1 = \tilde{n}_3 = 1$ in Eq. (26). With this simplification, the coefficient in front of the exponential becomes $\frac{4\tilde{n}_2}{(\tilde{n}_s + 1)^2}$, where we have change the subscript \tilde{n}_2 to \tilde{n}_s for convenience. Furthermore, we can set $\tilde{n}_s = n_s(\omega)$ for \tilde{t}_{jk} and solve Eq. (26) for $\tilde{n}_s = n_s(\omega) + i\kappa_s(\omega)$ in the exponential. Here, $n_s(\omega)$ is the index of refraction of the sample, and $\kappa_s(\omega)$ its extinction coefficient. This approximation is justified by the fact that the sample absorption is negligible in the Fresnel transmission coefficient compared to

the exponential term and is thus used in the data analysis here described. We obtain:

$$\tilde{H}(\omega) = \frac{4n_s(\omega)}{(n_s(\omega) + 1)^2} e^{i(\omega d/c)(\bar{n}_s - 1)} = \frac{4n_s(\omega)}{(n_s(\omega) + 1)^2} e^{i(\omega d/c)(n_s(\omega) - 1)} e^{-(\omega d/c)\kappa_s(\omega)} \quad (27)$$

Taking the modulus and phase of Eq. (27) leads to:

$$\Phi[\tilde{H}(\omega)] = \left(\frac{\omega d}{c}\right)(n_s(\omega) - 1) \rightarrow n_s(\omega) = 1 + \frac{c}{\omega d} \Phi[\tilde{H}(\omega)] \quad (28)$$

$$|\tilde{H}(\omega)| = \frac{4n_s(\omega)}{(n_s(\omega) + 1)^2} e^{-(\omega d/c)\kappa_s(\omega)} \rightarrow \kappa_s(\omega) = -\frac{c}{\omega d} \ln \left[\frac{(n_s(\omega) + 1)^2}{4n_s(\omega)} |\tilde{H}(\omega)| \right] \quad (29)$$

We can also re-write this result in terms of the absorption coefficient $\alpha(\omega)$ of the sample as:

$$n(\omega) = 1 + \frac{c}{\omega d} \Phi[\tilde{H}(\omega)] \quad (30)$$

$$\alpha(\omega) = \frac{2\omega}{c} \kappa(\omega) = -\frac{2}{d} \ln \left[\frac{(n(\omega) + 1)^2}{4n(\omega)} |\tilde{H}(\omega)| \right] \quad (31)$$

where we have dropped the subscript s for convenience. In conclusion, by Fourier transforming $\tilde{E}_r(t)$ and $\tilde{E}_s(t)$, which are obtained experimentally, the transfer function $\tilde{H}(\omega)$ can be calculated as $\tilde{E}_s(\omega)/\tilde{E}_r(\omega)$, and $n(\omega)$ and $\alpha(\omega)$ follow from Eqs. (30) and (31), respectively.

Data availability

Data that support the findings of this study are available from the corresponding author upon reasonable request.

Code availability

Codes that support the findings of this study are available from the corresponding author upon reasonable request.

Received: 11 August 2023; Accepted: 8 March 2024;

Published online: 22 March 2024

References

- Dicke, R. H. Coherence in spontaneous radiation processes. *Phys. Rev.* **93**, 99–110 (1954).
- Garraway, B. M. The Dicke model in quantum optics: Dicke model revisited. *Philos. Trans. Royal Soc. A* **369**, 1137–1155 (2011).
- Cong, K. et al. Dicke superradiance in solids. *J. Opt. Soc. Am. B* **33**, C80–C101 (2016).
- Forn-Díaz, P., Lamata, L., Rico, E., Kono, J. & Solano, E. Ultrastrong coupling regimes of light-matter interaction. *Rev. Mod. Phys.* **91**, 025005 (2019).
- Frisk Kockum, A., Miranowicz, A., De Liberato, S., Savasta, S. & Nori, F. Ultrastrong coupling between light and matter. *Nat. Rev. Phys.* **1**, 19–40 (2019).
- Hepp, K. & Lieb, E. H. On the superradiant phase transition for molecules in a quantized radiation field: the Dicke maser model. *Ann. Phys.* **76**, 360–404 (1973).
- Wang, Y. K. & Hioe, F. T. Phase transition in the Dicke model of superradiance. *Phys. Rev. A* **7**, 831–836 (1973).
- Lambert, N., Emary, C. & Brandes, T. Entanglement and the phase transition in single-mode superradiance. *Phys. Rev. Lett.* **92**, 073602 (2004).
- Artoni, M. & Birman, J. L. Quantum-optical properties of polariton waves. *Phys. Rev. B* **44**, 3736–3756 (1991).
- Makihara, T. et al. Ultrastrong magnon-magnon coupling dominated by antiresonant interactions. *Nat. Commun.* **12**, 3115 (2021).
- Hayashida, K. et al. Perfect intrinsic squeezing at the superradiant phase transition critical point. *Sci. Rep.* **13**, 2526 (2023).
- Emary, C. & Brandes, T. Quantum chaos triggered by precursors of a quantum phase transition: the Dicke model. *Phys. Rev. Lett.* **90**, 044101 (2003).
- Friedberg, R. & Hartmann, S. R. Temporal evolution of superradiance in a small sphere. *Phys. Rev. A* **10**, 1728–1739 (1974).
- Lawande, S. V., Jagatap, B. N. & Puri, R. R. Laser phase and amplitude fluctuations in the fluorescent Dicke model of interacting atoms. *J. Phys. B: At. Mol. Phys.* **18**, 1711 (1985).
- Lee, C. F. & Johnson, N. F. First-order superradiant phase transitions in a multiqubit cavity system. *Phys. Rev. Lett.* **93**, 083001 (2004).
- Chen, Q.-H., Liu, T., Zhang, Y.-Y. & Wang, K.-L. Quantum phase transitions in coupled two-level atoms in a single-mode cavity. *Phys. Rev. A* **82**, 053841 (2010).
- Yang, L.-P. & Jacob, Z. Quantum critical detector: amplifying weak signals using discontinuous quantum phase transitions. *Opt. Express* **27**, 10482–10494 (2019).
- Herrera Romero, R., Bastarrachea-Magnani, M. A. & Linares, R. Critical phenomena in light-matter systems with collective matter interactions. *Entropy* **24**, 1198 (2022).
- Zhao, X.-Q., Liu, N. & Liang, J.-Q. First-order quantum phase transition for Dicke model induced by atom-atom interaction. *Commun. Theor. Phys.* **67**, 511 (2017).
- Nie, J., Huang, X. & Yi, X. Critical properties of entanglement in the Dicke model with the dipole-dipole interactions. *Opt. Commun.* **282**, 1478–1481 (2009).
- Chen, G., Zhao, D. & Chen, Z. Quantum phase transition for the Dicke model with the dipole-dipole interactions. *J. Phys. B: At., Mol. Opt. Phys.* **39**, 3315 (2006).
- Wang, Q. Quantum chaos in the extended Dicke model. *Entropy* **24**, 1415 (2022).
- Robles Robles, R. A., Chilingaryan, S. A., Rodríguez-Lara, B. M. & Lee, R.-K. Ground state in the finite Dicke model for interacting qubits. *Phys. Rev. A* **91**, 033819 (2015).
- Rodríguez, J. P. J., Chilingaryan, S. A. & Rodríguez-Lara, B. M. Critical phenomena in an extended Dicke model. *Phys. Rev. A* **98**, 043805 (2018).
- Chen, G., Chen, Z. & Liang, J.-Q. Ground-state properties for coupled Bose-Einstein condensates inside a cavity quantum electrodynamics. *Europhys. Lett.* **80**, 40004 (2007).
- Rodríguez-Lara, B. M. & Lee, R.-K. Classical dynamics of a two-species condensate driven by a quantum field. *Phys. Rev. E* **84**, 016225 (2011).
- Zhang, Y. et al. Quantum phases in circuit QED with a superconducting qubit array. *Sci. Rep.* **4**, 4083 (2014).
- Tian, L. Circuit QED and sudden phase switching in a superconducting qubit array. *Phys. Rev. Lett.* **105**, 167001 (2010).
- White, R. L. Review of recent work on the magnetic and spectroscopic properties of the rare-earth orthoferrites. *J. Appl. Phys.* **40**, 1061–1069 (1969).
- Li, X. et al. Observation of Dicke cooperativity in magnetic interactions. *Science* **361**, 794–797 (2018).
- Zic, M. P. et al. Coupled spin waves and crystalline electric field levels in candidate multiferroic ErFeO₃. *J. Appl. Phys.* **130**, 014102 (2021).
- Deng, G. et al. The magnetic structures and transitions of a potential multiferroic orthoferrite ErFeO₃. *J. Appl. Phys.* **117**, 164105 (2015).
- Klochian, V., Kovtun, N. & Khmara, V. Low-temperature spin configuration of iron ions in erbium orthoferrite. *JETP* **41**, 357 (1975).
- Bamba, M., Li, X., Marquez Peraca, N. & Kono, J. Magnonic superradiant phase transition. *Commun. Phys.* **5**, 3 (2022).
- Li, X., Kim, D., Liu, Y. & Kono, J. Terahertz spin dynamics in rare-earth orthoferrites. *Photonics Insights* **1**, R05 (2022).

36. Kadomtseva, A. M., Krynetskii, I. B. & Matveev, V. M. Nature of the spontaneous and field-induced low-temperature orientational transitions in erbium orthoferrite. *JETP* **52**, 732 (1980).
 37. Dan'shin, N. K., Derkachenko, V. N., Kovtun, N. M. & Sdvizhkov, M. A. Metamagnetic phase transition in ErFeO_3 . *Sov. Phys. Solid State* **28**, 1461–1464 (1986).
 38. Dudko, K. L., Eremenko, V. V. & Fridman, V. M. Magnetic stratification during flipping of antiferromagnetic manganese fluoride sublattices. *JETP* **34**, 362–367 (1972).
 39. Zhu, L., Garst, M., Rosch, A. & Si, Q. Universally diverging grüneisen parameter and the magnetocaloric effect close to quantum critical points. *Phys. Rev. Lett.* **91**, 066404 (2003).
 40. Garst, M. & Rosch, A. Sign change of the grüneisen parameter and magnetocaloric effect near quantum critical points. *Phys. Rev. B* **72**, 205129 (2005).
 41. Jaime, M., Kim, K. H., Jorge, G., McCall, S. & Mydosh, J. A. High magnetic field studies of the hidden order transition in URu_2Si_2 . *Phys. Rev. Lett.* **89**, 287201 (2002).
 42. Romero-Muñiz, C., Ipus, J., Blázquez, J., Franco, V. & Conde, A. Influence of the demagnetizing factor on the magnetocaloric effect: critical scaling and numerical simulations. *Appl. Phys. Lett.* **104**, 252405 (2014).
 43. Moya, J. M. et al. Field-induced quantum critical point in the itinerant antiferromagnet Ti_3Cu_4 . *Commun. Phys.* **5**, 136 (2022).
 44. Belov, K. P., Zvezdin, A. K., Kadomtseva, A. M. & Levitin, R. Z. Spin-reorientation transitions in rare-earth magnets. *Sov. Phys. Usp.* **19**, 574–596 (1976).
 45. Balbashov, A., Kozlov, G., Mukhin, A. & Prokhorov, A. In *High Frequency Processes in Magnetic Materials* 56–98 (1995).
 46. Dan'shin, N. K., Kramarchuk, G. G. & Sdvizhkov, M. A. Observation of a soft mode and energy gaps during spontaneous spin reversal in YbFeO_3 . *JETP Lett.* **44**, 107–109 (1986).
 47. Kim, D. et al. Observation of the magnonic Dicke superradiant phase transition. Preprint at <https://doi.org/10.48550/arXiv.2401.01873> (2024).
 48. Zvezdin, A. K., Muchin, A. A. & Popov, A. I. Magnetic-structure instability resulting from the intersection of energy levels. *JETP Lett.* **23**, 240 (1976).
 49. Belov, K. P., Zvezdin, A. K. & Mukhin, A. A. Magnetic phase transitions in terbium orthoferrite. *Sov. Phys. JETP* **49**, 557–562 (1979).
 50. Rohn, J., Hörmann, M., Genes, C. & Schmidt, K. P. Ising model in a light-induced quantized transverse field. *Phys. Rev. Res.* **2**, 023131 (2020).
 51. Xu, Y. & Pu, H. Emergent universality in a quantum tricritical Dicke model. *Phys. Rev. Lett.* **122**, 193201 (2019).
 52. Altland, A. & Haake, F. Quantum chaos and effective thermalization. *Phys. Rev. Lett.* **108**, 073601 (2012).
 53. Bamba, M., Li, X. & Kono, J. in *Ultrafast Phenomena and Nanophotonics XXIII*, Vol. 10916 (eds. Betz, M. & Elezzabi, A. Y.) 1091605 (SPIE, 2019).
 54. Herrmann, G. Resonance and high frequency susceptibility in canted antiferromagnetic substances. *J. Phys. Chem. Solids* **24**, 597–606 (1963).
 55. Fisher, M. E. Relation between the specific heat and susceptibility of an antiferromagnet. *Philos. Mag.* **7**, 1731–1743 (1962).
 56. Naftaly, M. *Terahertz Metrology* (Artech House, 2015).
 57. Duvillaret, L., Garet, F. & Coutaz, J.-L. A reliable method for extraction of material parameters in terahertz time-domain spectroscopy. *IEEE J. Sel. Top. Quantum Electron.* **2**, 739–746 (1996).
- Foundation (through Grant No. 11520), and the Robert A. Welch Foundation (through Grant No. C-1509). X.L. acknowledges support from the Caltech Postdoctoral Prize Fellowship and the IQIM. S.C. is grateful for financial support from the National Natural Science Foundation of China (NSFC, No. 12374116), and the Science and Technology Commission of Shanghai Municipality (No. 21JC1402600). M.B. acknowledges support from the JST PRESTO program (Grant JPMJPR1767) and Japan Society for the Promotion of Science (Grant JPJSJRP20221202). J.M.M. and E.M. were supported by NSF Grant No. DMR 1903741 and the Robert A. Welch Foundation Grant No. C-2114. A.H.N. was supported by the Robert A. Welch Foundation (through Grant No. C-1818) and the US National Science Foundation (through Grant No. DMR-1917511). P.D. was supported by U.S. DOE BES DE-SC0012311. C.-L.H. is grateful for financial support from the National Science and Technology in Taiwan (NSTC 112-2124-M-006-011).

Author contributions

N.M.P. performed THz measurements and analyzed all THz data under the guidance and supervision of X.L. and J.K. J.M.M., C.-L.H., and E.M. performed magnetization and MCE measurements and data analysis and discussed the results with N.M.P., X.L., D.K., and J.K. K.H. and M.B. calculated spin resonance frequencies, spin configurations, oscillator strengths, and mean-field phase diagrams. M.B. supervised K.H. in the theoretical modeling. X.M. grew, cut, and characterized the high-quality ErFeO_3 single crystals used in the experiments under the guidance of S.C. K.J.N., and P.D. performed additional Laue diffraction measurements. D.F.P., H.P., and A.H.N. contributed to the theoretical analysis. N.M.P., X.L., J.M.M., K.H., D.K., M.B., and J.K. wrote the manuscript. All authors discussed the results and commented on the manuscript.

Competing interests

The authors declare no competing interests.

Additional information

Supplementary information The online version contains supplementary material available at <https://doi.org/10.1038/s43246-024-00479-3>.

Correspondence and requests for materials should be addressed to Xinwei Li, Shixun Cao, Motoaki Bamba or Junichiro Kono.

Peer review information *Communications Materials* thanks the anonymous reviewers for their contribution to the peer review of this work. Primary Handling Editor: Aldo Isidori.

Reprints and permissions information is available at <http://www.nature.com/reprints>

Publisher's note Springer Nature remains neutral with regard to jurisdictional claims in published maps and institutional affiliations.

Open Access This article is licensed under a Creative Commons Attribution 4.0 International License, which permits use, sharing, adaptation, distribution and reproduction in any medium or format, as long as you give appropriate credit to the original author(s) and the source, provide a link to the Creative Commons licence, and indicate if changes were made. The images or other third party material in this article are included in the article's Creative Commons licence, unless indicated otherwise in a credit line to the material. If material is not included in the article's Creative Commons licence and your intended use is not permitted by statutory regulation or exceeds the permitted use, you will need to obtain permission directly from the copyright holder. To view a copy of this licence, visit <http://creativecommons.org/licenses/by/4.0/>.

© The Author(s) 2024

Acknowledgements

We thank Shiming Lei, Andrey Baydin, Takuma Makihara, Fuyang Tay, and Timothy Noe for useful discussions. J.K. acknowledges support from the U.S. Army Research Office (through Award No. W911NF2110157), the W. M. Keck Foundation (through Award No. 995764), the Gordon and Betty Moore